Vortex-induced Vibration of Risers with Staggered Buoyancy Modules of Small Aspect Ratio

Ang Li*[a], Baiheng Wu*[b], Dixia Fan**[c]

[a]*School of Naval Architecture, Ocean and Civil Engineering, Shanghai Jiao Tong University, Shanghai 200240, China*
[b]*Department of Ocean Operations and Civil Engineering, Norwegian University of Science and Technology (NTNU), Larsgårdsvegen 2, 6009, Ålesund, Norway*
[c]*Department of Mechanical and Materials Engineering, Queen's University, Kingston, Ontario, K7L 3N6, Canada*

Abstract

Vortex-induced vibration (VIV) is one of the critical design considerations for the offshore riser and pipeline system. Significant research effort has been devoted to better understanding and predicting riser VIV. Compared to the bare uniform riser configuration, the attached staggered buoyancy modules of a small aspect ratio will extensively alter riser hydrodynamic characters, and hence the riser dynamic response. In the current study, experiments were performed on forced inline (IL)-crossflow (CF) combined vibration of a rigid cylinder with staggered modules (module to bare cylinder diameter and length ratio of 2.5 and 1.0.) as well as self-induced vibration of two flexible models with 100% and 50% buoyancy module coverage ratios. From the rigid model experiment, positive regions for lift coefficient in the phase of velocity (C_{lv}) for both riser and buoyancy module induced vibration are observed. The result indicates potential power-in excitation from both riser and buoyancy modules, which is later confirmed by the bi-frequency and bi-modal vibration from the flexible cylinder experiment. Furthermore, several other phenomena have been reported, including low reduced frequency for buoyancy module induced motion, the phase between CF and IL trajectory, and buoyancy module VIV suppression ability, emphasizing the connection between the rigid and flexible cylinder experiment.

Keywords: VIV, flexible riser, cross-flow, inline, buoyancy modules

1. Introduction

Vortex-Induced Vibration (VIV) is a ubiquitous phenomenon caused by shedding vortices behind bluff bodies. VIV induced by ocean currents and waves, if not considered, will

*Equally contributed first author
**Corresponding author
Email addresses: greatang@sjtu.edu.cn (Ang Li*), baiheng.wu@ntnu.no (Baiheng Wu*), dixia.fan@queensu.ca (Dixia Fan**)

generate extensive fatigue damage in riser systems [1]. And therefore, a significant research effort has been devoted to the understanding of riser VIV mechanism [2] and the prediction of its occurrence [3, 4]. One of the key factors in determining VIV is the structural shape, and, as a matter of fact, sometimes even a slight change of the shape will significantly affect the vortex formation pattern, and hence its coupled structural dynamic response [5, 6].

For risers in the deep water (larger than 1000m), staggered buoyancy modules will often be installed to help to provide additional lift force and therefore avoiding the excessive tension load in the riser due to its own weight [7, 8]. Meanwhile, buoyancy modules have also been widely used for risers to maintain a lazy wave format [9]. However, compared to the bare uniform riser section, the structural shape of the riser with staggered buoyancy modules will be altered as the buoyancy module diameter usually is 2.5-5 times larger than the riser diameter. Inevitably, the vortex formation may vastly change behind the structure; hence different VIV responses for the riser with buoyancy modules [10, 11, 12]. Questions, therefore, have been raised [7, 9] on whether the dynamic response will be dominated by the riser induced or buoyancy modules induced motion, or how the different coverage ratios between the buoyancy modules and riser will affect the dynamic response, etc.

In the previous research [13, 14, 15, 16], several experiments have been conducted on the flexible cylinder with buoyancy modules of aspect ratio from 4 to 6, and the finding allows the modeling of the riser with such buoyancy modules simply as cylinders with smaller and larger diameters staggered together [3]. However, this principle does not apply to the new form of buoyancy modules with an aspect ratio of 1 [10], as the hydrodynamics, the vortex shedding, etc., will be considerably altered for the cylinder with small aspect ratios [17].

Therefore, in the current study, to understand the hydrodynamic performance of the riser with buoyancy modules of a small aspect ratio, experiments have been conducted systematically on both rigid and flexible cylinders with staggered modules (module aspect ratio is 1.0, and module to bare cylinder diameter and length ratio are fixed at Dr = 2.5 and Lr = 1.0). Cross-flow (CF) and inline (IL) combined forced vibration experiments have been performed on the rigid model to determine its hydrodynamic coefficients [18] and construct a comprehensive hydrodynamic database [19, 20] for flexible cylinder VIV predictions [21, 22, 23]. In addition, using the underwater optical tracking system [24, 25], two flexible models of different coverage ratios have been tested to investigate its self-induced vibration.

The rest of the paper is organized as follows: In Section 2, a detailed description of the experimental setup and model construction is provided for both the rigid cylinder forced vibration and flexible cylinder free vibration experiments; We then in Section 3 present the result of the hydrodynamic coefficient acquired through the rigid cylinder experiment and their relationship with the different prescribed motion parameter; Section 4 discusses the several phenomena observed in the flexible cylinder free vibrations, including the bi-frequency and bi-modal vibration pattern, sectional CF and IL phase effect and buoyancy module VIV suppression ability, with an emphasis on the connection between the rigid and flexible cylinder experiment; At last, we conclude our major findings in Section 5.

2. Experiment Description

2.1. Rigid Model Forced Vibration Experiments

The forced vibration experiments of the rigid model with staggered modules have been conducted at MIT Tow Tank [26] to update the hydrodynamic database applied in the semi-empirical programs. The experiment aimed to help the industry to have a more precise prediction for VIV on the riser with a small aspect ratio buoyancy module. Meanwhile, it gave a comprehensive insight into the vortex force of the oscillating cylinder with staggered modules of a small aspect ratio compared with the self-induced vibration experiments.

2.1.1. Two Sets of Experiments with Different Rigid Models

First, to understand the VIV hydrodynamic contribution from bare riser or buoyancy modules, two different sets of experiments: the central riser referred experiments (CRR), and the buoyancy module referred experiments (BMR) were conducted. In the CRR set, the experiment parameters, such as the dimensionless amplitudes and the reduced velocity, were chosen based on the diameter of the central riser (d). In contrast, in the BMR set, the parameters were based on the diameter of the buoyancy modules (D).

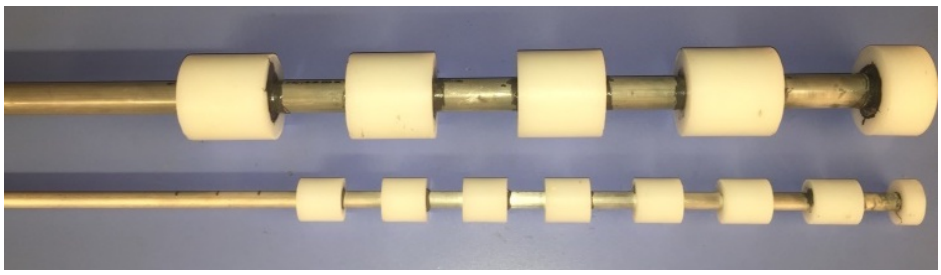

Figure 1: Physical rigid models occupied in the experiments
Upper: CRR model; Lower: BMR model

To guarantee adequate stabilized vibrating cycles due to the limitation of the towing length, two physical models of different scales as Fig. 1 were fabricated for the CRR and BMR sets of experiments separately. The model with larger diameters was used in the CRR set, while the smaller model was used in the BMR set. Detailed geometric parameters of the two models are shown in Table 1.

2.1.2. Experimental Parameters

In the forced vibration experiment, designated motions were defined as $y = A_y cos(2\pi f_y t)$ in CF direction while $x = A_x cos(2\pi f_x t + \theta)$ in IL direction, and the vibration frequency f_x was set to be twice as f_y. And in the two experiment sets, the dimensionless parameters $A_y D$, $A_x D$ and U_r were defined in Eq. 1 and Eq. 2. Special attention is needed that $A_x D$ and $A_y D$ have been non-dimensionalized by two different characteristic diameters of D in the BMR test and d in the CRR test.

For BMR set,

$$A_y D = \frac{A_y}{D} \qquad A_x D = \frac{A_x}{D} \qquad U_r = \frac{U}{fD} \tag{1}$$

Parameters	CRR set	BMR set
Diameter of Buoyancy Module (D)	63.5mm	31.8mm
Diameter of Central Riser (d)	25.4mm	12.7mm
Length of Buoyancy Module (L)	63.5mm	31.8mm
Length of Central Riser (l)	63.5mm	31.8mm
Dimensionless Amplitude of CF Vibration	A_yD: 0, 0.15, 0.3, 0.5 ,0.75, 1	
Dimensionless Amplitude of IL Vibration	A_xD: 0, 0.05, 0.1, 0.15, 0.2, 0.25, 0.3	
Reduced Velocity U_r	U_r: 6, 8, 10	
Phase Angle θ	$[0, 7\pi/4]$, step as $\pi/4$	

Table 1: The geometric parameters and definition of experimental parameters

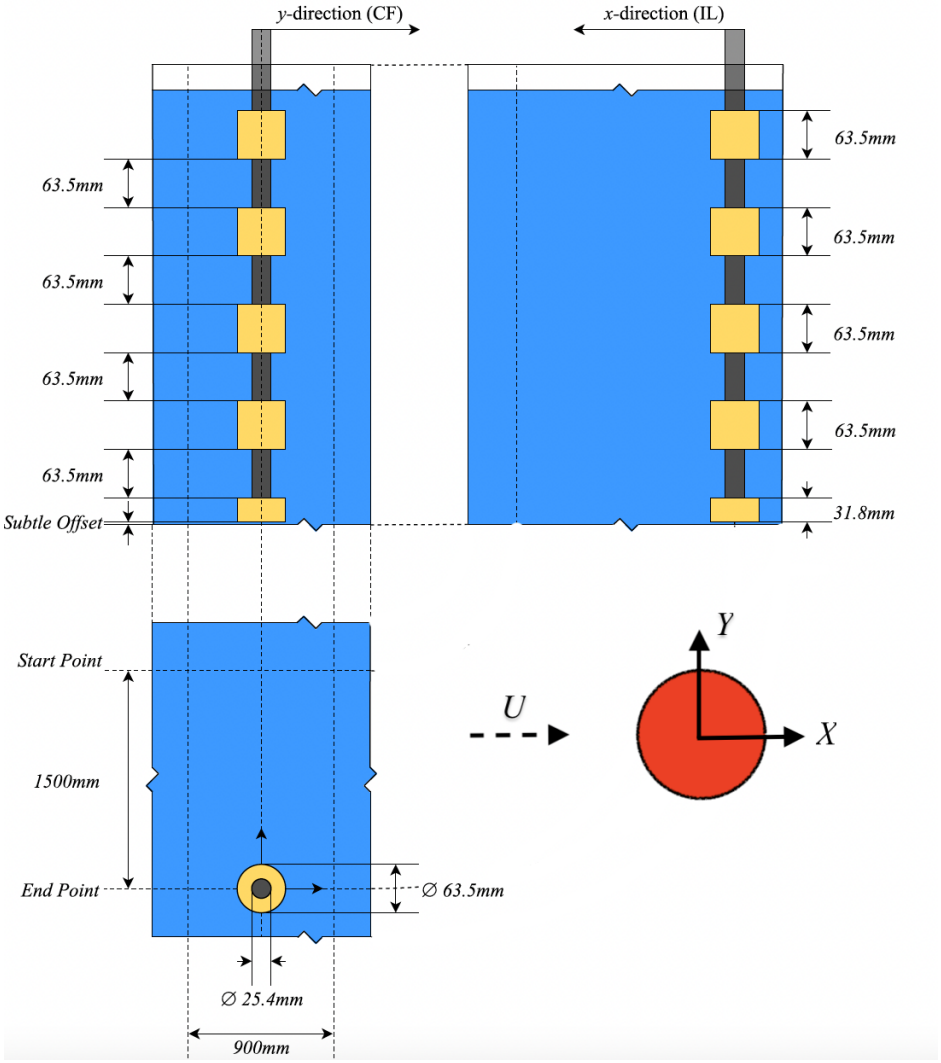

Figure 2: Rigid model (CRR) experiments setup in the tank. Right bottom subfigure shows the direction of the flow and positive directions of the force.

For CRR set,

$$A_yD = \frac{A_y}{d} \qquad A_xD = \frac{A_x}{d} \qquad U_r = \frac{U}{fd} \tag{2}$$

The forced vibration experiments contained stationary cases (amplitudes are 0 in both directions), one-dimensional vibrating cases (amplitude is 0 in either CF or IL directions), and CF-IL coupled cases. And the dimensionless amplitudes in CF direction A_yD were chosen as 0, 0.15, 0.3, 0.5, 0.75 and 1, and in IL direction, the dimensionless amplitudes of 0, 0.05, 0.1, 0.15, 0.2, 0.25 and 0.3 were chosen for A_xD. Based on previous research on the riser VIVs [27], in both sets of experiments, the phase angle θ between CF and IL direction was chosen from 0 to $7\pi/4$ with an incremental of $\pi/4$, and the reduced velocities U_r were chosen as 6, 8 and 10, i.e., and namely the reduced frequencies F_r as 0.167, 0.125, 0.100 correspondingly.

2.1.3. Experimental Apparatus

The forced vibration experiments on rigid risers were conducted in the small towing tank at MIT with an effective towing length of 1.20m and a width of 0.90m. The water depth applied in these sets of experiments was set as 0.63m. It is shown in Fig. 2 the configuration of how the CRR model was assembled in the tank.

The ATI 6-Axis Gamma Force Transducer was installed on the top of the model, connecting to the towing carriage. The hydro force and the forced motion trajectory were measured and recorded simultaneously.

2.1.4. Hydrodynamic Coefficients

Corresponding hydrodynamic coefficients were calculated from the measured force and prescribed motion, and they are clearly defined in this section. (The notations of these coefficients follow the same convention as in the Dahl's work [28].)

The mean drag force coefficient is defined in Eq. 3,

$$C_d = \frac{\overline{F^{IL}}}{\frac{1}{2}\rho U^2 S}, \tag{3}$$

where $\overline{F^{IL}}$ is the mean of the measured force in IL direction. S is the projected area of the model on the plane orthogonal to the flow direction. ρ is the flow density and U is the towing velocity. The lift force coefficient in phase of velocity C_{lv} is defined in Eq. 4.

$$C_{lv} = \frac{F_0^{CF} sin\phi_l}{\frac{1}{2}\rho U^2 S}, \tag{4}$$

where ϕ_l is the phase angle between CF motion and Lift force, and F_0^{CF} is the amplitude of the measured force in CF direction. The fluctuating drag force coefficient in phase of velocity C_{dv} is defined in Eq. 5.

$$C_{dv} = \frac{F_0^{IL} sin\phi_d}{\frac{1}{2}\rho U^2 S}, \tag{5}$$

where ϕ_d is the phase angle between IL motion and fluctuating drag force, F_0^{IL} is the amplitude of the measured fluctuating force in IL direction. The added mass coefficient of CF motion C_{my} and IL motion C_{mx} are defined in Eq. 6 and Eq. 7.

$$C_{my} = \frac{-F_0^{CF} cos\phi_l}{\rho \Delta A_y {\omega_y}^2}, \tag{6}$$

$$C_{mx} = \frac{-F_0^{IL} cos\phi_d}{\rho \Delta A_x {\omega_x}^2}, \tag{7}$$

where Δ is the modal fluid displacement. It should be noted that when there is vortex shedding, due to the variation of the relative motion between the shedding vortex and cylinder motion, the effective added mass coefficient may be altered considerably compared the potential added mass coefficient.

2.2. Flexible Model Self Induced Vibration Experiments

2.2.1. Flexible Model Description

Using the same configuration as the rigid model, the flexible model selects two coverage ratios of 100% and 50% (the length of the riser section with buoyancy modules to the total riser length). The core flexible riser model was molded via urethane rubber with an embedded fishing line, providing additional axial strength while keeping a low bending stiffness. Compared to the applied tension, the bending stiffness of the urethane rubber model was considered a negligible contribution to the model's natural frequency and modal shape. Hence, the model displayed a string-like vibration behavior. The attached buoyancy modules were made by rigid low-density polyethylene cylinder and then stuck on the riser model in a staggered configuration, which results in the mass per unit length (μ) of 0.175kg/m in the riser section and 0.860kg/m in the buoyancy module section. The first modal natural frequency (f_{n1}) of the model with full coverage in the still water is found to be 0.647Hz, and the higher modal natural frequency is the integer of f_{n1}, as the model is string dominated. However, it should be noted, when the towing velocity increase, the tension applied to the model also increases, which will lead to an increase of the natural frequency. The detailed model properties are listed in Table 2.

2.2.2. Experimental Apparatus and Measurement Technique

The flexible model experiment was performed at the MIT tow tank, and the total setup is shown in Fig. 3. Two foil-shape holders were fixed on the supporting beam with the model installed on the bottom of the holder, allowing tension adjustment and measurement with an underwater load cell. The total water depth is set to be 1.2m, and the immerse depth of the flexible cylinder model is chosen to be 0.6m. Four cameras were installed over 80d downstream of the model to measure CF vibration, while six cameras were installed 50d above the model to measure IL vibration. At the same time, four 1500-lumen underwater lights were installed to provide enough camera background lighting. Corresponding image processing and motion tracking code have been developed to capture and follow the trajectory of either white or black markers [24]. The following Fig. 4 demonstrates a sketch of the

general camera setup in the experiment, and Fig. 5 displays a sample frame of the raw and processed images for one of the ten cameras. Notice that we set the middle of the flexible model as the origin.

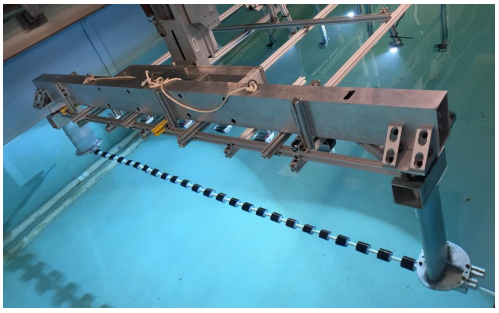

Figure 3: Experimental setup of flexible riser model in the MIT Tow Tank

Total length	2050mm	
Coverage Ratio	50%, 100%	
Geometric Parameters	**Riser**	**Buoyancy Module**
Outer Diameter	12.7mm	31.8mm
Section Length	31.8mm	31.8mm
μ	0.175kg/m	0.860kg/m
f_{n1}	2050mm	

Table 2: Detailed geometric parameters and physical properties of flexible riser and buoyancy modules attached

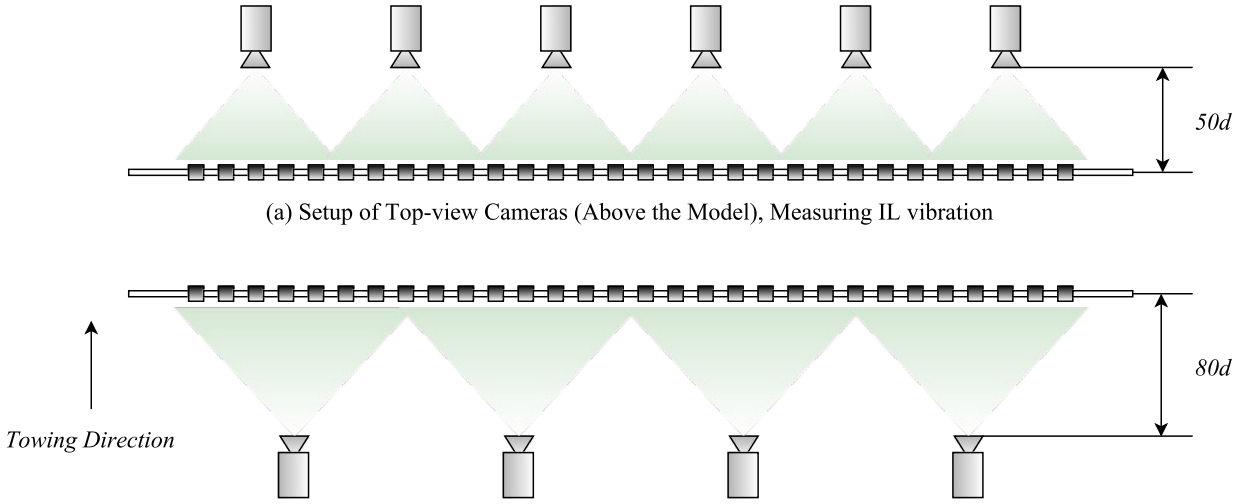

(a) Setup of Top-view Cameras (Above the Model), Measuring IL vibration

(b) Setup of Back-view Cameras (Downstrean the Model), Measuring CF vibration

Figure 4: Camera arrangement in IL (a) and CF (b) direction.

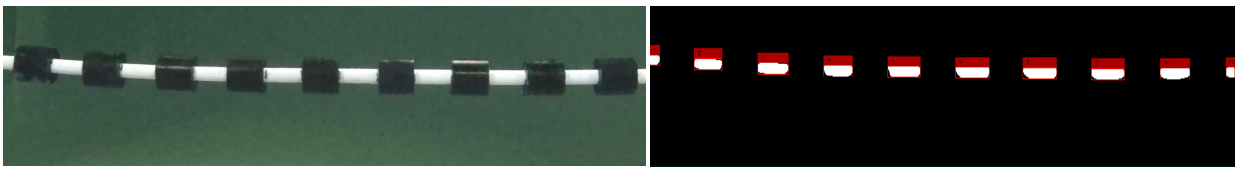

(a) Sample image from one camera for the CF measurement

(b) Processed image with specific algorithm

Figure 5: Sample case of tracked motions: a. Sample in CF direction; b. Processed image (the red bounding box shows the ability to capture the motion of the white markers.).

3. Forced Vibration of the Rigid Model

The hydrodynamic coefficients defined in 2.1.4 have been first briefly reported by Le Garrec et al., [26]. In this section, some notable trends are concluded, and some interesting phenomena are pointed out for further discussion. Attention is paid to the discrepancies between two sets of experiments (CRR and BMR).

3.1. The Mean Drag Force Coefficient C_d

Fig. 6a gives the entire database of C_d from CRR set of experiments. In each sub-figure in Fig. 6a, it shows how the mean drag force coefficients C_d changes with A_yD (x-axis) and A_xD (y-axis) at one reduced velocity and phase angle. Such trends are found similar to those in the Bare rigid cylinder forced vibration experiments. In general, from the contour map, we conclude that C_d tends to increase with the decrease of U_r and the amplitude increase in both CF and IL direction. And the values in the current experiment range from 1.2 to 2.5.

The distribution of C_d in the BMR set of experiments has a similar trend and is averagely larger than in the CRR set. The values in the current experiment range from 1.2 to 3. In Fig. 7, case of A_yD and A_xD is picked to be 0.75 and 0.1 as a representative for both CRR (green) and BMR (red) sets. Fig. 7 shows that the mean drag coefficient in the BMR set may hold a different trend but is usually larger than that in the CRR set. Since the amplitudes in the BMR set are based on the diameter of buoyancy modules, i.e., the amplitudes are originally larger than those in CRR set, this might contribute to the divergence of the C_d's values in two models.

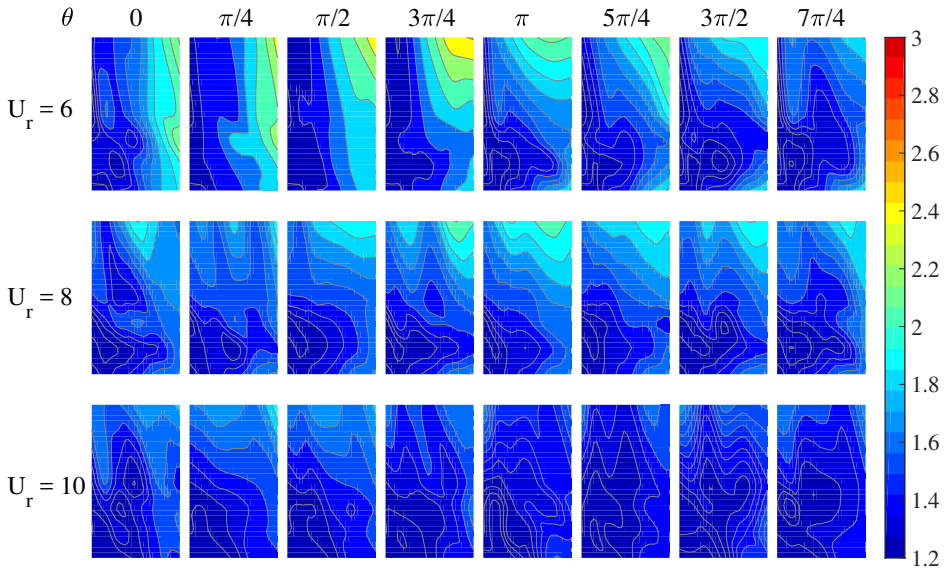

(a) In CRR set

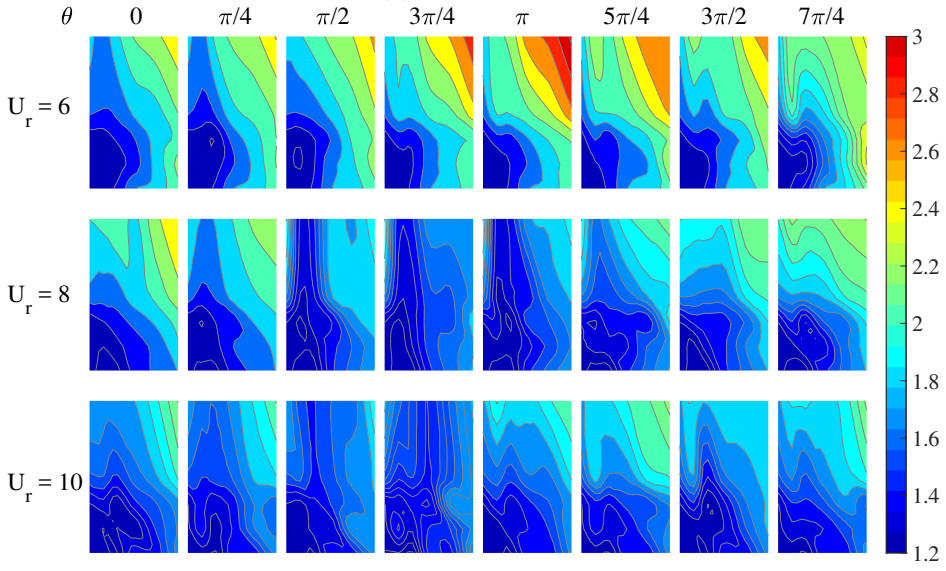

(b) In BMR set

Figure 6: Contour of all C_d values from both sets of experiments. The x-axis ($A_y D$) ranges from 0 to 1, and the y-axis ($A_x D$) ranges from 0 to 0.3.

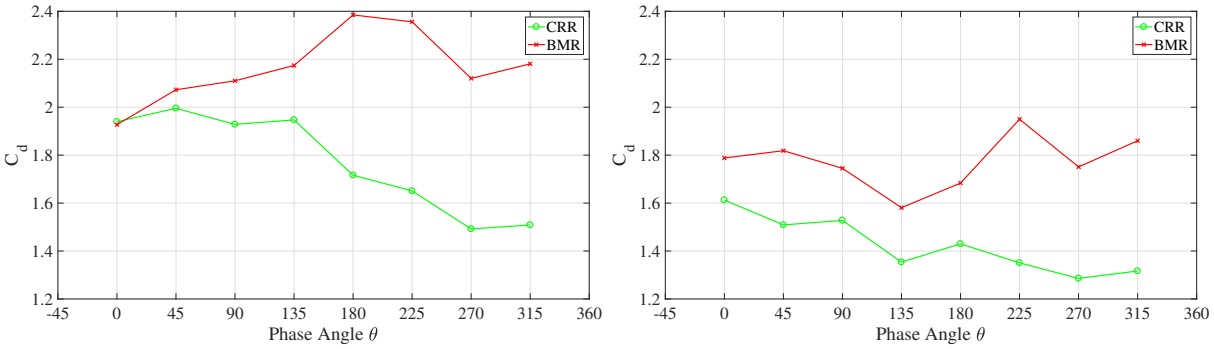

(a) $U_r = 6$ (b) $U_r = 10$

Figure 7: Trend of C_d along with θ ($A_xD = 0.1$,$A_yD = 0.75$)

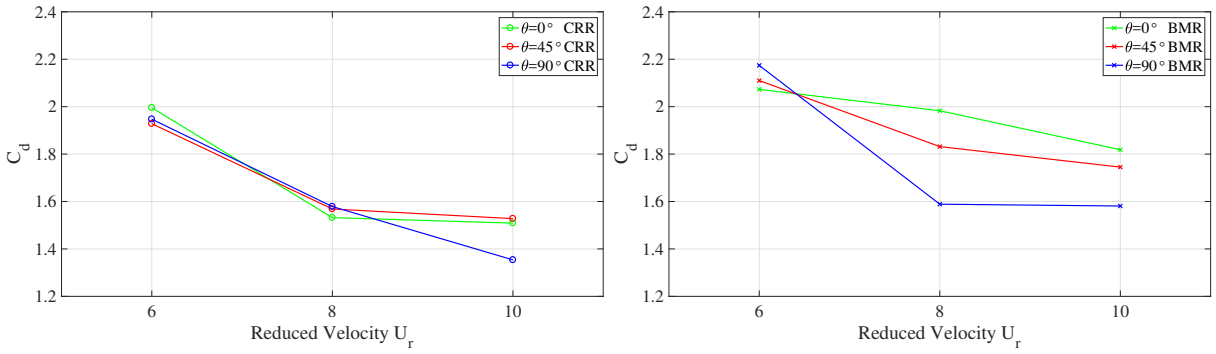

(a) In CRR set (b) In BMR set

Figure 8: Trend of C_d along with U_r ($A_xD = 0.1$, $A_yD = 0.75$)

Fig. 8 (a) and (b) show how the C_d changes against the reduced velocity U_r. It is demonstrated that C_d decreases with the increase of the reduced velocity. And from Fig. 8, it can also be seen that BMR's model would, in general, obtain a larger mean drag coefficient than CRR's model when comparing Fig. 8 (a) and (b).

3.2. The Lift Force Coefficient in Phase of Velocity C_{lv}

The lift force coefficient in the phase of velocity C_{lv} calls for special attention as it directly reveals the possible occurrence of VIV in CF direction [29].

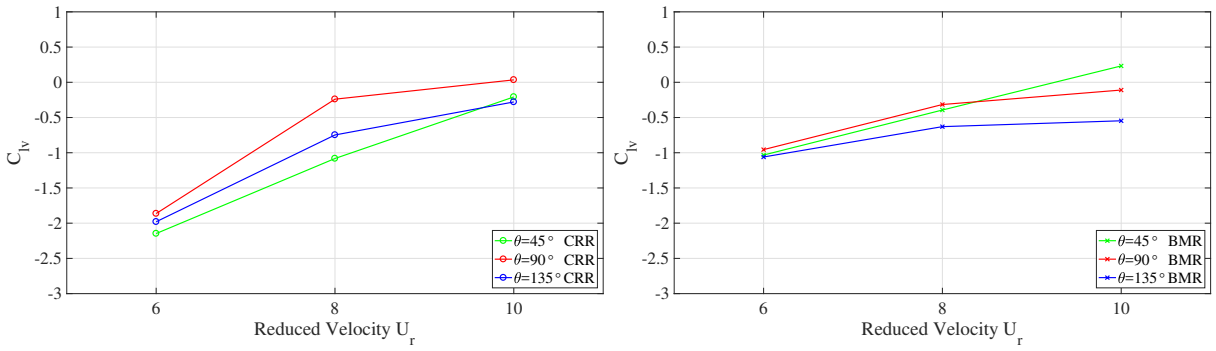

(a) In CRR set (b) In BMR set

Figure 9: Trend of C_{lv} along with U_r ($A_xD = 0.15$, $A_yD = 0.75$)

Fig. 9 reveals the trend how C_{lv} changes against the reduced velocity for fixed dimensionless amplitude of $A_xD = 0.1$, $A_yD = 0.75$. In both CRR and BMR sets of experiments, C_{lv} increases with the increase of U_r, but the slopes vary among the cases of motions at different phase angle θ. Moreover, according to Fig. 9, positive C_{lv} values appear when U_r is 10 in both sets of experiments, and the occurrence of the positive regions can be more clearly observed in Fig. 10.

In Fig. 10, bold black line separates the positive and negative C_{lv} region. From Fig. 10, It can be found that positive area of C_{lv} values appear in both sets of experiments, which

suggests potential VIV excitation from both bare riser and buoyancy module. Emphasis should be made that the chosen reduced velocity refers to different diameters in CRR and BMR experiments, which means there is no overlapping of the experimental parameters between two sets of the experiments. For instance, as for BRR sets, the designated reduced velocities refers to the module diameter, and if they are calculated based on the central riser diameter, the corresponding reduced velocities become 2.4, 3.2, and 4, i.e., when VIV in CF direction may not happen for the bare cylinder [28], and vise versa for CRR sets.

Furthermore, it is also revealed that in BMR set, the positive area of C_{lv} is in general qualitatively larger than that in the CRR set, suggesting module-induced motion may overwhelm riser-induced motion when combined. In addition, we see that in both BMR and CRR sets, C_{lv} has a strong dependence on the phase angle that large positive region is found for θ from 0 to π, corresponding to the counter-clockwise trajectory of CF and IL motion. This strong phase angle θ dependence can also be spotted in the bare cylinder experiment [28].

3.3. The Fluctuating Drag Force Coefficient in Phase of Velocity C_{dv}

Similar to the lift coefficient in the phase of velocity C_{lv}, the fluctuating drag coefficient in the phase of velocity C_{dv} is used to predict the possible occurrence of VIV in IL direction [30]. Two contour figures shown in Fig. 11 are selected to represent the general distribution trend. First of all, the values of C_{dv} decrease sharply along with the increasing A_xD. Meanwhile, positive values are observed in mainly BMR sets for small A_xD and large A_yD combination. However, no positive value is found for the CRR set in Fig. 11 (there are only scattered several positive points in the entire CRR experiment, and is not shown in the selected sub-figure). The result suggests that the buoyancy modules are more inclined to contribute to the vibration in IL direction than the central riser section. It will keep a small module induced amplitude motion, as when A_xD is large, energy will be dissipated from structure to fluid, indicated by the negative C_{dv}.

3.4. The Added Mass Coefficient C_{my} and C_{mx}

When VIV happens, the true natural frequency of the system may be extensively altered due to the variation of the added mass coefficient. As Eq. 8, it shows the CF and IL true natural frequency of a self induced rigid model when taking added mass coefficient into consideration, in which m^* is the mass ratio of the system (structural mass divided by the displacement fluid mass) and ω_n is the natural frequency of the system in air. It reveals that the added mass would have a significant effect, especially for the low mass ratio structure [31].

$$\omega_{n,CF/IL} = \omega_n \sqrt{\frac{m^*}{m^* + C_{my/mx}}} \tag{8}$$

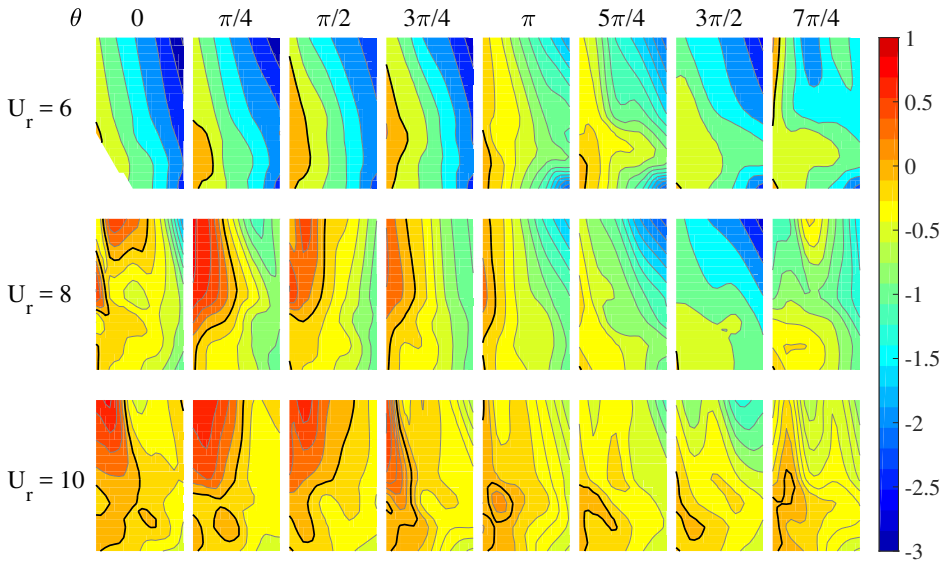

(a) In CRR set

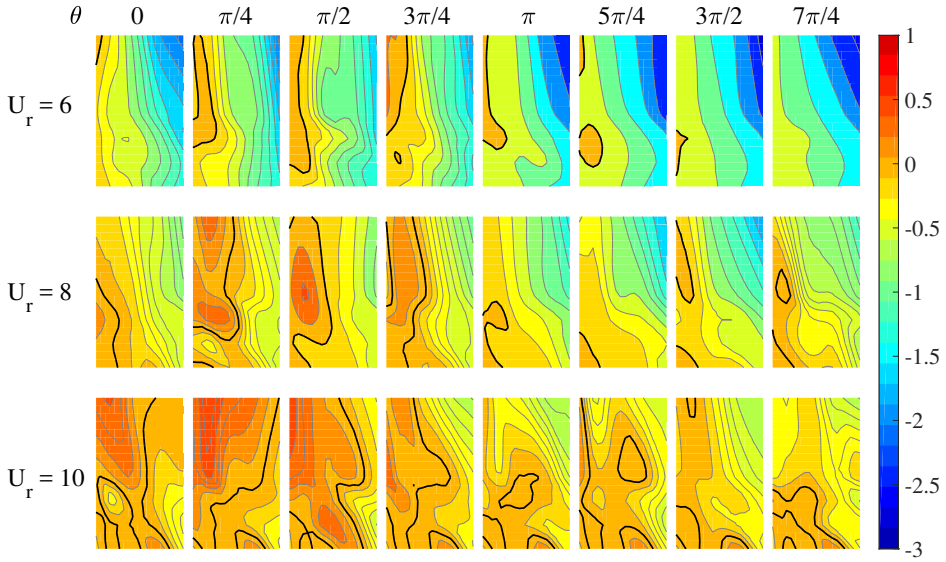

(b) In BMR set

Figure 10: Contour of all C_{lv} values from both sets of experiments. The x-axis (A_yD) ranges from 0 to 1, and the y-axis (A_xD) ranges from 0 to 0.3.

Fig. 12 again selects the case of $A_xD = 0.15$,$A_yD = 0.75$ to represent the trend of C_{my} against reduced velocity. In the CRR set, C_{my} lightly fluctuates with the change of the reduced velocity. In contrast, the BMR set obviously decreases with the increasing reduced velocity and even reaches negative values. Fig. 13 represents the trend of C_{mx} against reduced velocity. C_{mx} shows a very similar trend as C_{my} that in CRR set, C_{mx} does not change much over the reduced velocity, while in BMR set, C_{mx} decrease with the increase of the reduced velocity and reaches a negative value at $U_r = 10$ for certain phase angle.

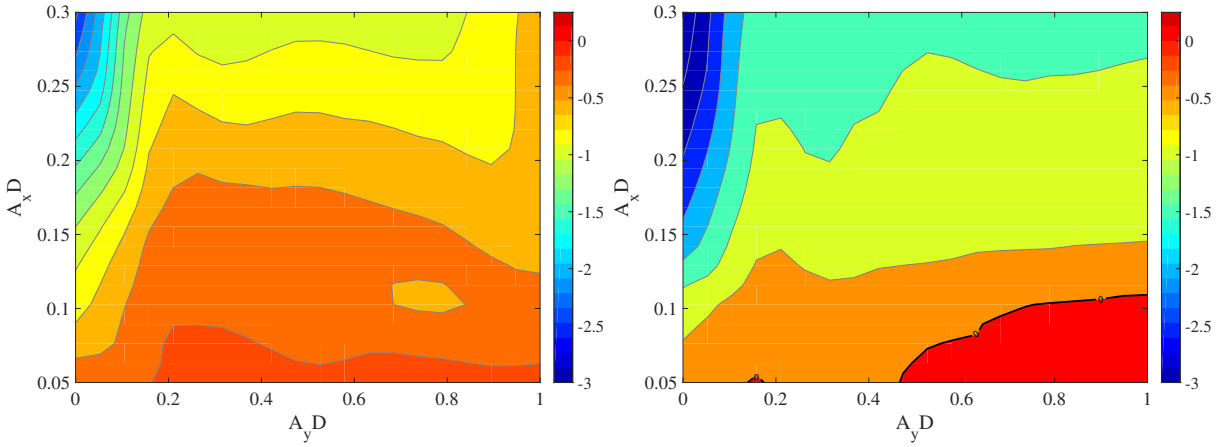

(a) In CRR set (b) In BMR set

Figure 11: Distribution of C_{dv} with A_xD and A_yD ($\theta = \pi/2$, $U_r = 10$)

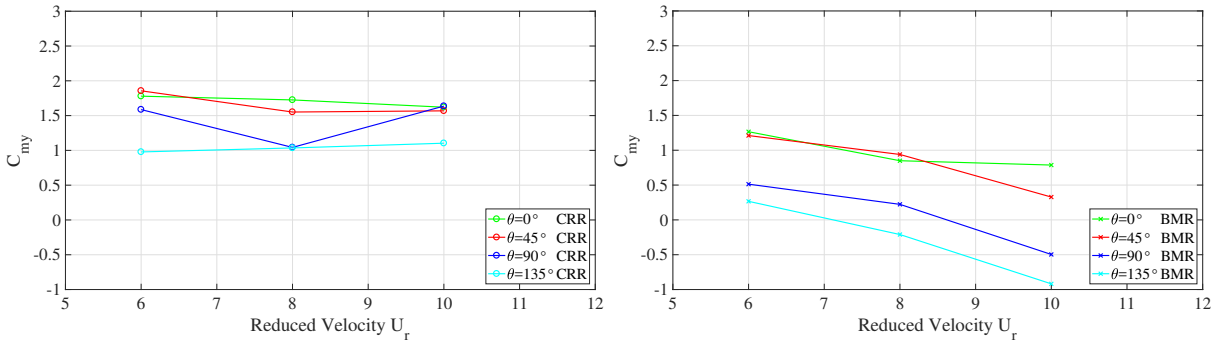

(a) In CRR set (b) In BMR set

Figure 12: Trend of C_{my} along with U_r ($A_xD = 0.15$,$A_yD = 0.75$)

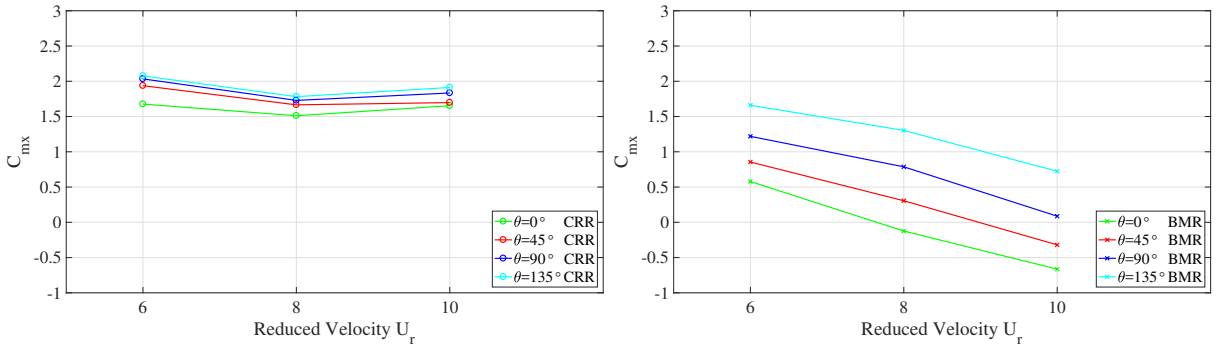

(a) In CRR set (b) In BMR set

Figure 13: Trend of C_{mx} along with U_r ($A_xD = 0.15$,$A_yD = 0.75$)

Furthermore, it is found that both C_{my} and C_{mx} have a strong correlation with the phase angle θ, which is shown in Fig. 14 for C_{my} and Fig. 15 for C_{mx}. From Fig. 14, it is

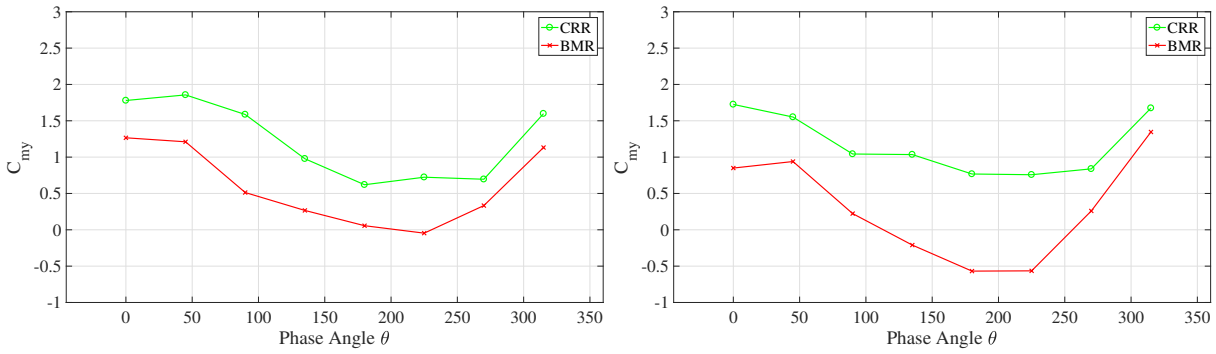

(a) $U_r = 6$ (b) $U_r = 8$

Figure 14: Trend of C_{my} along with θ ($A_xD = 0.15$,$A_yD = 0.75$)

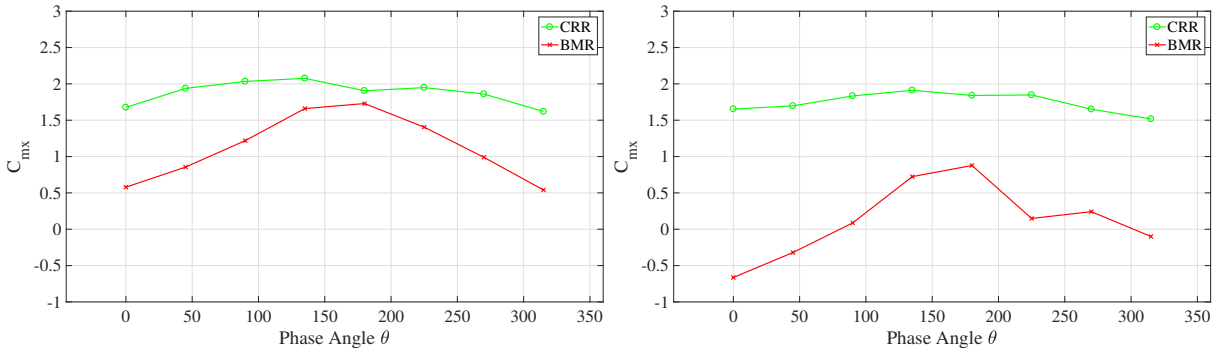

(a) $U_r = 6$ (b) $U_r = 10$

Figure 15: Trend of C_{mx} along with θ ($A_xD = 0.15$,$A_yD = 0.75$)

found that although there is a difference between the CRR and the BMR sets for various reduced velocities, the value of C_{my} reaches the lowest for both CRR and BMR sets around phase angle of π, when CF and IL trajectory switches from counter-clockwise to clockwise. However, from Fig. 15, value of C_{mx} reaches its highest for CRR and BMR when θ is around π. In addition, we can also see that compared to the large variation of the C_{mx} over θ in BMR experiments, C_{mx} for CRR sets fluctuates lightly between 1.6 and 2.1.

4. Self-induced Vibration of the Flexible Model

4.1. Model Frequency Response

In Fig. 16, it shows the power spectral density (PSD) analysis of the CF(blue) and IL(red) motion at 7 points along the flexible model of 100% coverage ratio for $U = 0.20m/s$. In CF direction, it is found that there are two distinctive components: lower frequency with larger amplitude of $0.768Hz$ and higher frequency with smaller amplitude of $2.81Hz$. Attention should be paid that these two frequencies do not have an integer relationship, and therefore the higher frequency is not simply a high harmonic term of the lower frequency. Such coexistence of the low and high-frequency components in the CF direction (non-integer

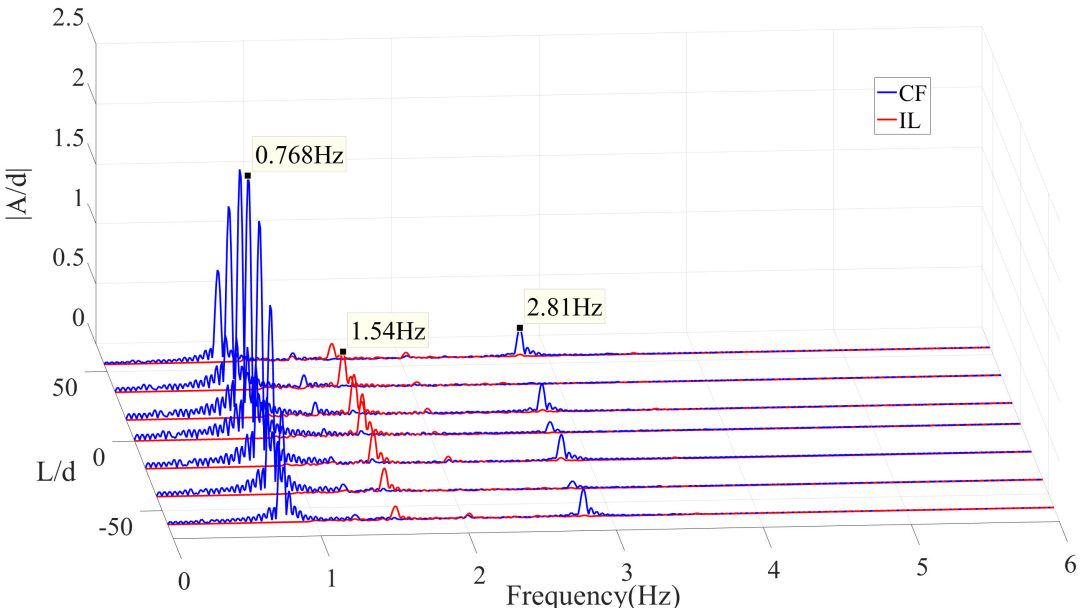

Figure 16: FFT Analysis of CF(blue) and IL(red) motion for $U = 0.20m/s$

relationship) can be found for all the current experiments. This can be explained that two frequencies in CF direction come from different sources that buoyancy module with larger diameter contributes to the lower frequency, larger amplitude vibration while central riser induced the higher frequency, smaller amplitude vibration. This is supported by the rigid forced vibration experiment in which positive C_{lv} regions can be found for both BMR and CRR sets. Hence, potentially, both riser and module-induced vibration may occur. Furthermore, in Fig. 16, it is also revealed that in the current experiment, IL displays a mono-frequency vibration with second harmonics of the CF low-frequency component, namely the module induced vibration. And, second harmonic term of the high frequency, riser CF vibration, is not found. This phenomenon again is supported by the rigid forced vibration experiment, in which a large positive C_{dv} region can be only spotted in the BMR set.

Picking out the peak frequencies from the PSD, reduced frequency F_r is plotted against flow velocity with reference diameter carefully selected to have reduced frequency fall in the reasonable VIV range from 0.1-0.2 (Here we use small diameter in $F_r^d = fd/U$) for high-frequency component and use large diameter in $F_r^d = fD/U$) for low frequency component), shown in Fig. 17. From the reduced frequency plot, a conclusion can be drawn that the buoyancy modules induce the low-frequency vibration. At the same time, the riser section contributes to the high-frequency vibration.

As for the F_r^d of the riser motion remains a value between 0.16 and 0.19, which is close to the bare flexible cylinder undergoing VIV in the uniform flow. However, reduced frequency is surprisingly low for the buoyancy module induced motion, with an average value around 0.12 and a minimum value of only 0.1 at U = 0.3m/s. The physical reason behind that remains

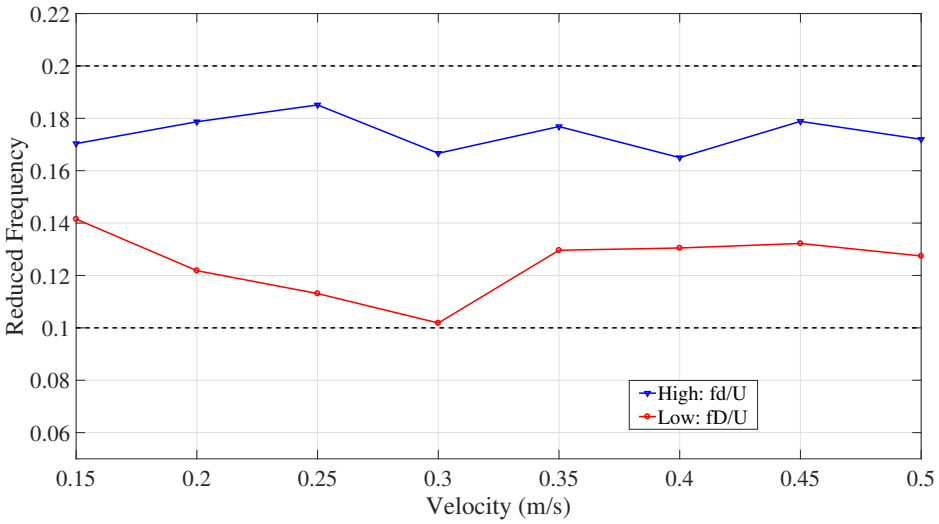

Figure 17: Reduced frequency V.S. velocity for flexible cylinder with 100% coverage ratio. Small diameter ($F_r^d = fd/U$) is used for high frequency components (blue) and large diameter ($F_r^D = fD/U$) is used for low frequency components (red).

unclear and calls for a more detailed examination through future research, including flow visualization. But this may be because the finite length of the buoyancy module (aspect ratio is 1.0) will change the vortex shedding pattern a lot. More importantly, it delivers us an important massage that when we construct the VIV hydrodynamic coefficient database by forced rigid cylinder vibration experiment, we need to extend one of the experiment parameter, the upper bound of the reduced velocity U_r (inverse of the F_r described here in the Fig. 17) from normally 8 [27] to an even larger number of at least 12 [32, 33].

4.2. Separation of the Multiple Frequency Vibration

Applied band-pass filter, the two frequency vibration components in CF direction are separated and plotted together in Fig. 18. From Fig. 18(a-c) it displays the total displacement, low frequency displacement and high frequency displacement from time 10s - 15s, and at the same time, it also plots in Fig. 18(d) the displacement overtime at location of L/d = 20 (denoted by white dash line in Fig. 18(a)), as well as, in Fig. 18(e), the time-frequency analysis on 18(d). The result shows that the two frequencies, instead of occupying different periods, coexist at the same time over the whole vibration. Like the lesson we learned from the low reduced frequency of the module-induced vibration, the result guides us to rethink the forced vibration for the rigid model. Instead of using a single frequency sinusoidal motion trajectory, multiple frequencies and amplitudes trajectory should be applied. Meanwhile, the coexisting low and high-frequency components will induce low and high modes that coexist at the same time as well, as shown in Fig. 18(b-c). $1/10^{th}$ highest peak of the total, low frequency and high frequency CF amplitude response are plotted in Fig. 19 for $U = 0.20m/s$ and $U = 0.50m/s$ cases. In the current experiment when $U = 0.20m/s$, the low frequency component leads to 1^{st} modal vibration, while the high frequency excites 4^{th} modal vibration, and for $U = 0.50m/s$, 2^{nd} and 7^{th} mode are excited separately in CF

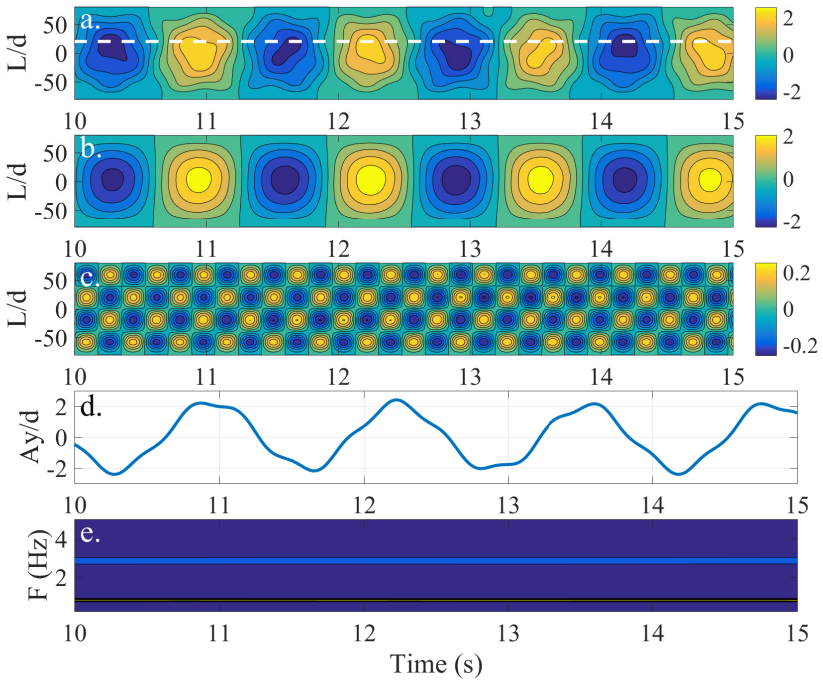

Figure 18: CF time displacement of flexible model with 100% coverage ratio for U = 0.2m/s (a: total displacement response; b: low frequency displacement response; c: High frequency displacement response; d: the displacement over time at location of L/d = 20; e: time frequency analysis).

direction. And at the same time, in the current experiment, the low-frequency component vibrates at a much larger amplitude than the high-frequency vibration. The low-frequency vibration (buoyancy module induced vibration) achieves the amplitude of 2-2.6 times of the riser diameter (around one buoyancy module diameter), while the high-frequency components (riser induced vibration) stays about 0.2-0.3 riser diameter, which is smaller, compared to the one diameter amplitude response of flexible cylinder VIV of the uniform cylinder in the uniform flow. And this result suggests that with the slow yet large-amplitude buoyancy module induced motion, the high-frequency riser induced motion keeps a small amplitude and, hence, can potentially increase fatigue life.

4.3. Added Mass Variation in CF and IL Direction: an Comparison between Flexible Model and Rigid Model Experiment

This section gives special attention to the phenomenon found in the flexible cylinder self-induced vibration and their connection to the result of the hydrodynamic coefficient acquired from the forced vibration of the rigid model.

In Fig. 20(a), it shows that IL has a 2^{nd} harmonic frequency component of $1.54Hz$, compared to the low-frequency component of $0.77Hz$ in CF direction (the measured nature frequency of the system in the still water is $0.81Hz$.). And yet the $1/10^{th}$ highest peak value of the CF and IL module induced displacement response in Fig. 20(b) reveals that, instead

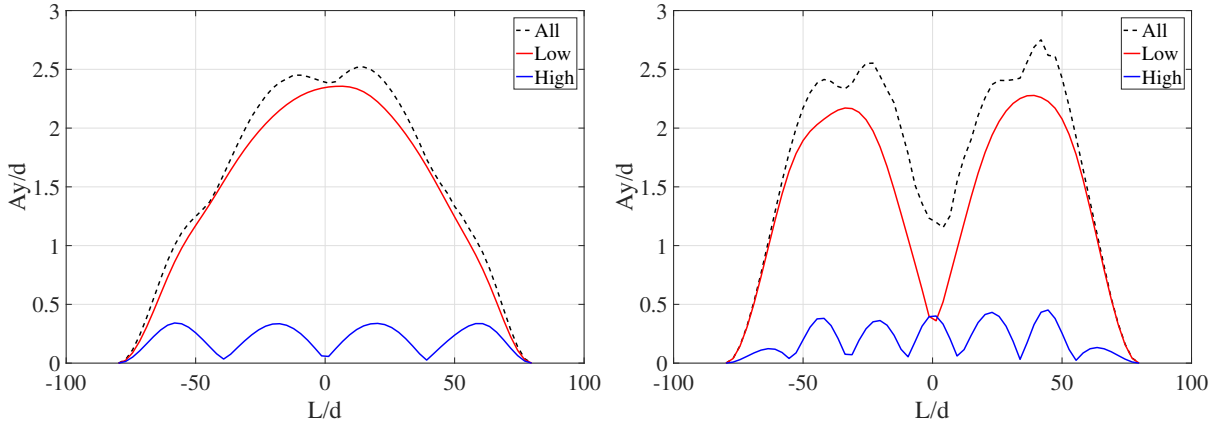

(a) $U = 0.20m/s$ (b) $U = 0.50m/s$

Figure 19: Separated $1/10^{th}$ highest CF amplitude response (dash line: total response; blue line: low frequency module induced response; red line: high frequency riser induced response).

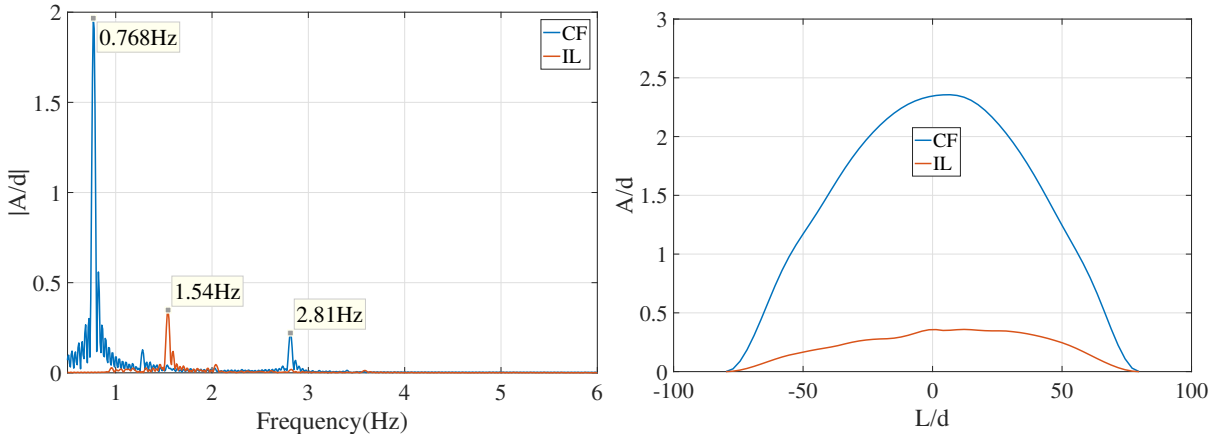

(a) PSD at $L/d = 30$ (b) CF and IL displacement

Figure 20: Separated $1/10^{th}$ highest CF amplitude response of flexible model with 100% coverage ratio (dash line: total response; blue line: low frequency module induced response; red line: high frequency riser induced response).

of 2^{nd} modal vibration in IL direction as expected, since the IL vibration frequency reaches almost 2^{nd} modal frequency (based on the tension dominated string model), both CF and IL still vibrate at 1^{st} mode. Such result indicts there must be an added mass variation in CF and IL direction that helps to alter the natural frequency in CF and IL direction to cater to the externally driven force frequencies, as stated in Eq. 8.

Analyzing CF and IL cross-sectional trajectory, we can see in Fig. 21, a clear counter clockwise figure-8 trajectory with phase angle θ around $\pi/4$ (In Fig. 21, flow direction points from right to left.) over the entire length of the model. Together with phase, frequency and displacement response in CF and IL direction, we will be able to locate the added mass coefficient C_{mx} and C_{my} from the rigid cylinder forced vibration experiments with the

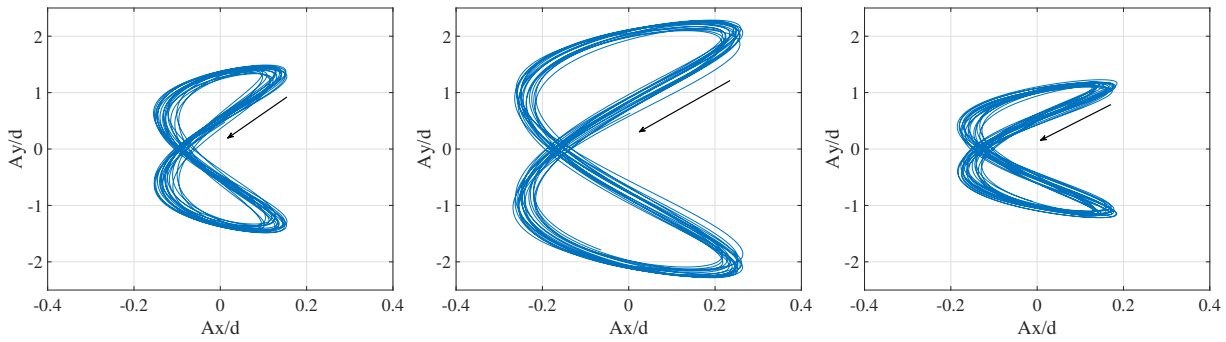

(a) $L/d = -40$ (b) $L/d = 5$ (c) $L/d = 50$

Figure 21: CF and IL cross-sectional trajectory along the span at $L/d = -40$ (a), $L/d = 5$ (b) and $L/d = 50$ (c) for the flexible cylinder with 100 % coverage ratio at $U = 0.2m/s$.

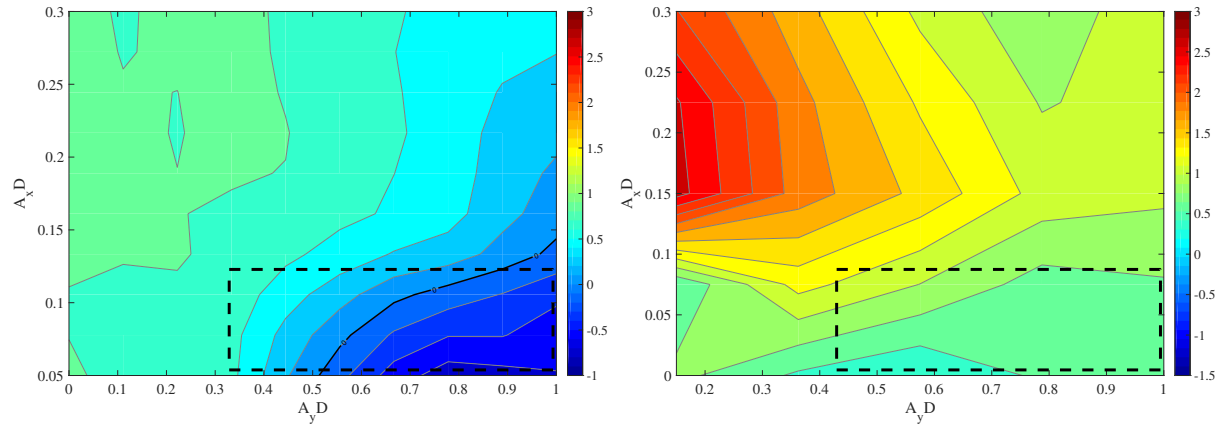

(a) C_{mx} (b) C_{my}

Figure 22: Added mass coefficient C_{mx} (a) and C_{my} (b) for $Ur = 8$ and $\theta = \pi/4$.

corresponding parameters. In Fig. 22, it shows the C_{mx} (Fig. 22(a)) and C_{my} (Fig. 22(b)) from BMR sets at $Ur = 8$ and $\theta = \pi/4$, and the dashed rectangle region points out the added mass coefficient C_{my} and C_{mx} over the flexible at $U = 0.20m/s$, based on rigid forced vibration. It is seen that at $Ur = 8$ and $\theta = \pi/4$ in BMR experiments, with large A_yD and small A_xD combination, C_{my} keeps an average value of 0.85, while C_{mx} reaches averagely negative value -0.6. And this will drive the natural frequency of the 1^{st} mode in CF and IL direction differently as $0.82Hz$ and $1.46Hz$, (based on the measured tension of 7.6N), and hence keep 1^{st} modal vibration in both CF and IL direction.

4.4. Buoyancy module VIV suppression effect on bare-section-induced vibrations

In the experiment of the self-induced vibration of the flexible cylinder with 50% coverage ratio, similar phenomena, such as bi-modal and bi-frequency response, have been observed. However, an additional phenomenon is identified: the buoyancy module can help reduce the high-frequency VIV contributed to the bare riser section.

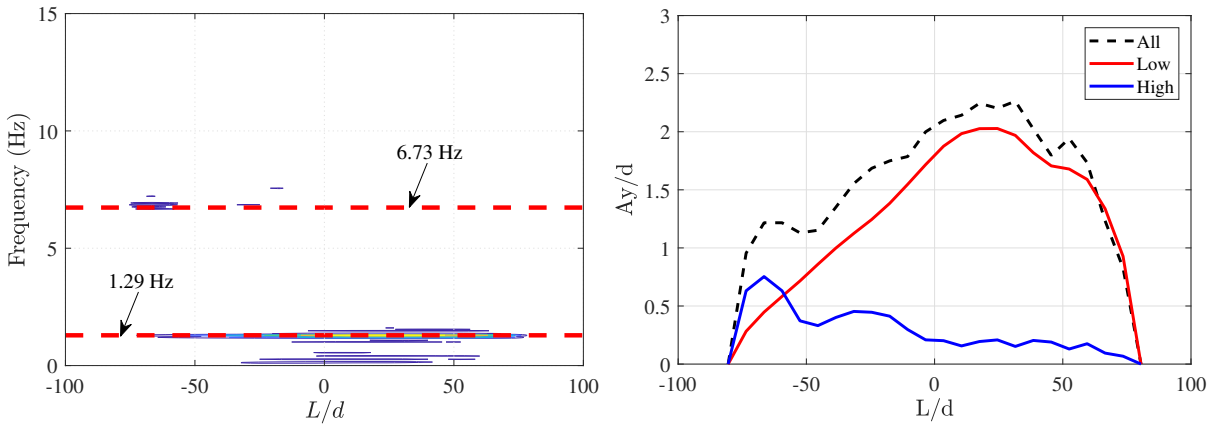

(a) PSD (b) CF and IL displacement

Figure 23: PSD of the FFT Analysis (a) and Separated $1/10^{th}$ highest CF amplitude response (b) for the flexible model with 50% coverage ratio at $U = 0.5m/s$. In (b): dash line: total response; red line: low frequency module induced response; blue line: high frequency riser induced response.

Taking the case of $U = 0.5m/s$ as an example, shown in Fig. 23 (a), the PSD result demonstrate the two co-existing frequency at 1.29Hz and 6.73Hz. After applying band-filter to separate low and high-frequency vibration components, the $1/10^{th}$ highest amplitude for total (black dashed line), low frequency (red line: induced by buoyancy module), and high frequency (blue line: induced by the bare riser section) for CF response are plotted in Fig. 23. It can be seen that in the negative half of the model span (where the bare riser section is), the high-frequency vibration amplitude has reached 0.7d, larger than those observed in the flexible cylinder with 100% coverage ratio (Fig. 20). However, the high-frequency vibration amplitude is significantly reduced in the section where the buoyancy module is. It can be seen that the amplitude of the high frequency traveling wave decreases continuously when it moves further into the buoyancy module covered area (from $L/d = 0$ to $L/d = 81$). Such a finding provides a promising riser design strategy that the buoyancy module with small aspect ratios can not only be used for weight compensation but also be applied to suppress the high-frequency VIVs contributed from the bare riser section in the high-speed current, normally close the free surface[34].

5. Conclusion

In the current research, we have experimentally studied the hydrodynamic performance of the riser with staggered buoyancy modules of small aspect ratio (L/D = 1.0, D/d = 2.5, and L/l = 1.0). Forced vibration experiments have been performed on two rigid models to acquire the hydrodynamic coefficient when the model is being forced into different trajectories. And flexible models with two different coverage ratios have been tested under different velocities to study their self-induced response.

The hydrodynamic coefficient database is constructed via rigid cylinder forced vibration based on either central riser diameter (d) or buoyancy module diameter (D). The result

reveals that positive regions for lift coefficient in the phase of velocity C_{lv} can be found in both CRR and BMR experiments, indicting both riser and buoyancy module induced vibration in CF direction may occur. However, the positive value of C_{dv} can be only spotted in BMR sets, suggesting in the IL direction, module-induced vibration may dominate the response. Furthermore, via experiment, we find that for force coefficient in the phase of velocity, C_{lv} and C_{dv}, as well as the added mass coefficient, C_{my} and C_{mx}, they all have a strong dependence on the phase angle θ between CF and IL motion. The positive region of C_{lv} is found mainly for the counter-clockwise trajectory, and C_{my} and C_{mx} reach local minimum/maximum when motion switching from counter-clockwise to clockwise.

The flexible model experiment displays a phenomenon of bi-frequency and bi-modal vibration in the CF direction, confirming results from the rigid model experiment that both riser and buoyancy module may induce vibration by themselves. Moreover, we show a connection between the flexible and rigid models. The added mass coefficients acquired in the rigid model experiments help explain the CF and IL vibration mode phenomenon in the flexible model experiment. However, results of the coexistence of the bi-frequency and the low reduced frequency F_r found for the module induced motion leave us an important lesson that higher reduced velocity, as well as the bi-frequency motion trajectories, are required for the rigid model forced vibration for future research to better predict the hydrodynamics of risers with staggered buoyancy modules of a small aspect ratio. Furthermore, the flexible cylinder with a 50% coverage ratio reveals that the buoyancy module with small aspect ratios can help suppress the high-frequency VIVs contributed from the bare riser section.

Acknowledgement

We wish to acknowledge the funding support of the research initiation grant provided by Queen's University and NERSC Discovery Grant.

References

[1] J. Wang, D. Fan, K. Lin, A review on flow-induced vibration of offshore circular cylinders, Journal of Hydrodynamics 32 (3) (2020) 415–440.

[2] Y. Xu, S. Fu, Y. Chen, Q. Zhong, D. Fan, Experimental investigation on vortex induced forces of oscillating cylinder at high reynolds number, Ocean Systems Engineering 3 (3) (2013) 167–180.

[3] M. Triantafyllou, G. Triantafyllou, Y. Tein, B. D. Ambrose, et al., Pragmatic riser VIV analysis, in: Offshore technology conference, Offshore Technology Conference, 1999.

[4] E. Passano, C. Larsen, H. Lie, J. Wu, VIVANA theory manual, Trondheim: MARINTEK Report.

[5] H. Zhu, Y. Gao, T. Zhou, Flow-induced vibration of a locally rough cylinder with two symmetrical strips attached on its surface: Effect of the location and shape of strips, Applied Ocean Research 72 (2018) 122–140.

[6] H. Zhu, W. Liu, Wake structure and evolution of flow over a finned circular cylinder, Physics of Fluids 33 (7) (2021) 073613.

[7] H. Lie, K. Mo, J. K. Vandiver, et al., VIV model test of a bare-and a staggered buoyancy riser in a rotating rig, in: Offshore Technology Conference, Offshore Technology Conference, 1998.

[8] H. Zheng, J. Wang, A numerical study on the vortex-induced vibration of flexible cylinders covered with differently placed buoyancy modules, Journal of Fluids and Structures 100 (2021) 103174.

[9] Z. Rao, J. K. Vandiver, V. Jhingran, VIV excitation competition between bare and buoyant segments of flexible cylinders, VIV Excitation Competition Between Bare and Buoyant Segments of Flexible Cylinders 7.
[10] D. Fan, M. Triantafyllou, Vortex induced vibration of riser with low span to diameter ratio buoyancy modules, in: The Twenty-seventh International Ocean and Polar Engineering Conference, 2017.
[11] C. Ji, Y. Cui, D. Xu, X. Yang, N. Srinil, Vortex-induced vibrations of dual-step cylinders with different diameter ratios in laminar flows, Physics of Fluids 31 (7) (2019) 073602.
[12] C. Tian, F. Jiang, B. Pettersen, H. I. Andersson, Vortex system around a step cylinder in a turbulent flow field, Physics of Fluids 33 (4) (2021) 045112.
[13] J. K. Vandiver, et al., Research challenges in the vortex-induced vibration prediction of marine risers, in: Offshore Technology Conference, Offshore Technology Conference, 1998.
[14] L. Li, S. Fu, J. Yang, T. Ren, X. Wang, Experimental investigation on vortex-induced vibration of risers with staggered buoyancy, in: International Conference on Offshore Mechanics and Arctic Engineering, Vol. 44397, 2011, pp. 51–59.
[15] S. M. Fang, J. M. Niedzwecki, S. Fu, R. Li, J. Yang, VIV response of a flexible cylinder with varied coverage by buoyancy elements and helical strakes, Marine Structures 39 (2014) 70–89.
[16] J. Wu, H. Lie, S. Fu, R. Baarholm, Y. Constantinides, VIV responses of riser with buoyancy elements: forced motion test and numerical prediction, in: International Conference on Offshore Mechanics and Arctic Engineering, Vol. 57649, American Society of Mechanical Engineers, 2017, p. V002T08A013.
[17] V. Jhingran, H. Zhang, H. Lie, H. Braaten, J. K. Vandiver, et al., Buoyancy spacing implications for fatigue damage due to vortex-induced vibrations on a steel lazy wave riser (SLWR), in: Offshore Technology Conference, Offshore Technology Conference, 2012.
[18] D. Fan, G. Jodin, T. Consi, L. Bonfiglio, Y. Ma, L. Keyes, G. E. Karniadakis, M. S. Triantafyllou, A robotic intelligent towing tank for learning complex fluid-structure dynamics, Science Robotics 4 (36).
[19] K. Lin, D. Fan, J. Wang, Dynamic response and hydrodynamic coefficients of a cylinder oscillating in crossflow with an upstream wake interference, Ocean Engineering 209 (2020) 107520.
[20] S. Rudy, D. Fan, J. d. A. Ferrandis, T. Sapsis, M. S. Triantafyllou, Learning optimal parametric hydrodynamic database for vortex-induced crossflow vibration prediction of both freely-mounted rigid and flexible cylinders, in: The 31st International Ocean and Polar Engineering Conference, OnePetro, 2021.
[21] Z. Wang, D. Fan, M. S. Triantafyllou, G. E. Karniadakis, A large-eddy simulation study on the similarity between free vibrations of a flexible cylinder and forced vibrations of a rigid cylinder, Journal of Fluids and Structures 101 (2021) 103223.
[22] K. Lin, J. Wang, D. Fan, M. S. Triantafyllou, Flow-induced cross-flow vibrations of long flexible cylinder with an upstream wake interference, Physics of Fluids 33 (6) (2021) 065104.
[23] Z. Wang, D. Fan, M. S. Triantafyllou, Illuminating the complex role of the added mass during vortex induced vibration, Physics of Fluids 33 (8) (2021) 085120.
[24] D. Fan, H. Du, M. Triantafyllou, Optical tracking measurement on vortex induced vibration of flexible riser with short-length buoyance module, in: APS Division of Fluid Dynamics Meeting Abstracts, 2016.
[25] D. Fan, B. Wu, D. Bachina, M. S. Triantafyllou, Vortex-induced vibration of a piggyback pipeline half buried in the seabed, Journal of Sound and Vibration 449 (2019) 182–195.
[26] J. Le Garrec, D. Fan, B. Wu, M. S. Triantafyllou, Experimental investigation of cross flow-inline coupled vortex-induced vibration on riser with finite length buoyancy module, in: OCEANS 2016 MTS/IEEE Monterey, IEEE, 2016, pp. 1–7.
[27] H. Zheng, J. M. Dahl, Y. Modarres-Sadeghi, M. S. Triantafyllou, Coupled inline-cross flow VIV hydrodynamic coefficients database, in: ASME 2014 33rd International Conference on Ocean, Offshore and Arctic Engineering, American Society of Mechanical Engineers, 2014, pp. V002T08A087–V002T08A087.
[28] J. J. M. Dahl, Vortex-induced vibration of a circular cylinder with combined in-line and cross-flow motion, Ph.D. thesis, Massachusetts Institute of Technology (2008).
[29] D. Fan, Z. Wang, M. S. Triantafyllou, G. E. Karniadakis, Mapping the properties of the vortex-induced

vibrations of flexible cylinders in uniform oncoming flow, Journal of Fluid Mechanics 881 (2019) 815–858.

[30] J. V. Ulveseter, S. Sævik, C. M. Larsen, Time domain model for calculation of pure in-line vortex-induced vibrations, Journal of Fluids and Structures 68 (2017) 158–173.

[31] K. Javadi, F. Kinai, On the turbulent flow structures over a short finite cylinder: numerical investigation, in: Proceedings of the International Conference on Heat Transfer and Fluid Flow, Praque, Czech Republic, 2014, p. 6.

[32] J. Dahl, F. Hover, M. Triantafyllou, Two-degree-of-freedom vortex-induced vibrations using a force assisted apparatus, Journal of Fluids and Structures 22 (6-7) (2006) 807–818.

[33] J. Dahl, F. Hover, M. Triantafyllou, O. Oakley, Dual resonance in vortex-induced vibrations at subcritical and supercritical reynolds numbers, Journal of Fluid Mechanics 643 (2010) 395–424.

[34] H. Marcollo, A. E. Potts, D. Johnstone, P. Pezet, P. Kurts, Drag reduction and VIV suppression behaviour of lgs technology integral to drilling riser buoyancy units, in: International Conference on Ocean, Offshore and Arctic Engineering 2016, American Society of Mechanical Engineers (ASME), 2016.